LETTER

doi:10.1038/nature12072

Optical magnetic imaging of living cells

D. Le Sage[1,2]*, K. Arai[3]*, D. R. Glenn[1,2,4]*, S. J. DeVience[5], L. M. Pham[6], L. Rahn-Lee[7], M. D. Lukin[2], A. Yacoby[2], A. Komeili[7] & R. L. Walsworth[1,2,4]

Magnetic imaging is a powerful tool for probing biological and physical systems. However, existing techniques either have poor spatial resolution compared to optical microscopy and are hence not generally applicable to imaging of sub-cellular structure (for example, magnetic resonance imaging[1]), or entail operating conditions that preclude application to living biological samples while providing submicrometre resolution (for example, scanning superconducting quantum interference device microscopy[2], electron holography[3] and magnetic resonance force microscopy[4]). Here we demonstrate magnetic imaging of living cells (magnetotactic bacteria) under ambient laboratory conditions and with sub-cellular spatial resolution (400 nanometres), using an optically detected magnetic field imaging array consisting of a nanometre-scale layer of nitrogen–vacancy colour centres implanted at the surface of a diamond chip. With the bacteria placed on the diamond surface, we optically probe the nitrogen–vacancy quantum spin states and rapidly reconstruct images of the vector components of the magnetic field created by chains of magnetic nanoparticles (magnetosomes) produced in the bacteria. We also spatially correlate these magnetic field maps with optical images acquired in the same apparatus. Wide-field microscopy allows parallel optical and magnetic imaging of multiple cells in a population with submicrometre resolution and a field of view in excess of 100 micrometres. Scanning electron microscope images of the bacteria confirm that the correlated optical and magnetic images can be used to locate and characterize the magnetosomes in each bacterium. Our results provide a new capability for imaging bio-magnetic structures in living cells under ambient conditions with high spatial resolution, and will enable the mapping of a wide range of magnetic signals within cells and cellular networks[5,6].

Nitrogen–vacancy (NV) colour centres in diamond (see Methods for details) enable nanometre-scale magnetic sensing and imaging under ambient conditions[7,8]. As recently shown using a variety of methods[6,9,10], NV centres within room-temperature diamond can be brought into close proximity (a few nanometres) of magnetic field sources of interest while maintaining long NV electronic spin coherence times (of the order of milliseconds), a large (about one Bohr magneton) Zeeman shift of the NV spin states, and optical preparation and readout of the NV spin. Recent demonstrations of NV-diamond magnetometry include high-precision sensing and submicrometre imaging of externally applied and controlled magnetic fields[6,9–11]; detection of electron[12] and nuclear[13–15] spins; and imaging of a single electron spin within a neighbouring diamond crystal with ~10 nm resolution[16]. However, a key challenge for NV-diamond magnetometry is submicrometre imaging of spins and magnetic nanoparticles located outside the diamond crystal and within a target of interest. Here we present the first such demonstration of NV-diamond imaging of the magnetic field distribution produced by a living biological specimen.

Magnetotactic bacteria (MTB) are of considerable interest as a model system for the study of molecular mechanisms of biomineralization[17,18] and have often been used for testing novel biomagnetic imaging modalities[3,19–21]. MTB form magnetosomes, membrane-bound organelles containing nanoparticles of magnetite (Fe_3O_4) or greigite (Fe_3S_4), that are arranged in chains with a net dipole moment, allowing the bacteria to orient and travel along geomagnetic field lines (magnetotaxis)[17,18]. Magnetic nanoparticles produced in the magnetosomes are chemically pure, single-domain monocrystalline ferrimagnets, with species-specific morphologies and strikingly uniform size distributions[17,18]. These features, combined with the ease of biofunctionalization and aqueous dispersion afforded by the magnetosome membrane[22], make synthesis of magnetic nanoparticles by MTB an attractive research area for various biomedical applications[18,22], including magnetic labelling, separation and drug delivery, as well as local hyperthermic cancer treatment and contrast enhancement in magnetic resonance imaging. For the NV-diamond bio-magnetic imaging demonstrations presented here (see Fig. 1), we used *Magnetospirillum magneticum* AMB-1, an MTB strain that forms magnetic nanoparticles with cubo-octahedral morphology and an average diameter of ~50 nm. (Figure 1c shows a

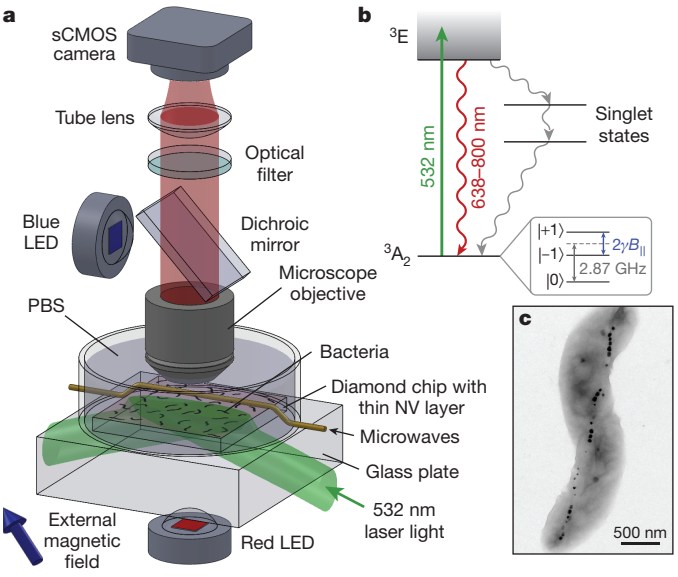

Figure 1 | Wide-field magnetic imaging microscope. a, Custom-built wide-field fluorescence microscope used for combined optical and magnetic imaging. Live magnetotactic bacteria (MTB) are placed in phosphate-buffered saline (PBS) on the surface of a diamond chip implanted with nitrogen–vacancy (NV) centres. Vector magnetic field images are derived from optically detected magnetic resonance (ODMR)[8–10] interrogation of NV centres excited by a totally-internally-reflected 532 nm laser beam, and spatially correlated with bright field optical images. See text for details. LED, light-emitting diode. **b**, Energy-level diagram of the NV centre; see Methods for details. **c**, Typical transmission electron microscope (TEM) image of an *M. magneticum* AMB-1 bacterium. Magnetite nanoparticles appear as spots of high electron density.

[1]Harvard-Smithsonian Center for Astrophysics, Cambridge, Massachusetts 02138, USA. [2]Department of Physics, Harvard University, Cambridge, Massachusetts 02138, USA. [3]Department of Physics, Massachusetts Institute of Technology, Cambridge, Massachusetts 02139, USA. [4]Center for Brain Science, Harvard University, Cambridge, Massachusetts 02138, USA. [5]Department of Chemistry and Chemical Biology, Harvard University, Cambridge, Massachusetts 02138, USA. [6]School of Engineering and Applied Science, Harvard University, Cambridge, Massachusetts 02138, USA. [7]Department of Plant and Microbial Biology, University of California Berkeley, Berkeley, California 94720, USA.
*These authors contributed equally to this work.

transmission electron microscopy image exhibiting the characteristic morphology of *M. magneticum* AMB-1, including a chain of magnetic nanoparticles distributed over the length of the cell. Gaps between nanoparticles are common in AMB-1 (ref. 23).)

We acquired correlated magnetic field and optical images of populations of MTB using the NV-diamond wide-field imager depicted schematically in Fig. 1a (ref. 6). The system was operated in two distinct configurations, one optimized for rapid magnetic imaging of living cells in a liquid medium, and the other for high-precision measurements of stable magnetic field patterns produced by dry bacteria on the diamond surface. In both cases, magnetic imaging was carried out using a pure diamond chip doped with a 10-nm-deep surface layer of NV centres. NV electronic spin states were optically polarized and interrogated with green illumination (wavelength $\lambda = 532$ nm), coherently manipulated using resonant microwave fields, and detected via spin-state-dependent fluorescence in the red (Fig. 1b). NV electronic spin resonance frequencies are Zeeman-shifted in the presence of a local external magnetic field (such as from magnetic nanoparticles in an MTB), allowing NV-fluorescence-based magnetometry by optically detected magnetic resonance (ODMR)[8–10]. Four independent ODMR measurements enabled determination of all vector components of the magnetic field within each imaging pixel (see Methods). For imaging of live samples, the green excitation beam was directed into the diamond chip at an angle greater than the critical angle for the diamond–water interface, resulting in total internal reflection of high-intensity green light within the diamond, while low-intensity red NV fluorescence passed freely to the objective and was imaged onto the sCMOS (scientific complementary metal-oxide semiconductor) camera (Fig. 1a). Cells at the diamond surface were thereby decoupled from high optical intensity, allowing NV magnetic imaging times up to several minutes while maintaining cellular viability. For magnetic imaging of dry bacteria, the green excitation beam could be configured in the same manner as for live/wet samples, or be allowed to pass directly through the sample, normal to the diamond surface, with comparable optical and magnetic imaging results.

We obtained optical images of the magnetic field distributions produced by multiple cells on the diamond surface across a wide field of view (100 μm × 30 μm) and with high spatial resolution (~400 nm) using a sCMOS camera (Fig. 2). We concurrently acquired bright-field optical images using red ($\lambda = 660$ nm) LED illumination to enable correlation of cell positions and morphology with the observed magnetic field patterns. Immediately following magnetic imaging, the MTB were stained and imaged in fluorescence under blue ($\lambda = 470$ nm) LED excitation to perform a bacterial viability assay (see Methods), using a conservative viability threshold that excluded non-viable bacteria with 99% certainty (see Supplementary Methods). Under appropriate imaging conditions, the magnetic field patterns produced by the MTB could be measured within 4 min with minimal cellular radiation exposure, such that a significant fraction of the MTB remained alive after magnetic and bright-field imaging. For example, ~44% of the MTB in the field of view shown in Fig. 2a, b were found to be viable after magnetic and bright-field imaging, compared to 54% viability for cells directly from culture. Many of these living MTB produced magnetic field signals with large signal-to-noise ratios (~10). For high-precision characterization of the bacterial magnetic fields and comparison to electron microscope images, we also carried out a series of measurements using dried MTB samples on the diamond surface, imaged using a high-numerical-aperture (high-NA) air objective (Fig. 2c, d). Relaxing the requirement of maintaining cellular viability allowed for longer magnetic image averaging times, with concomitant reduction in photon shot-noise. Also, elimination of both the poly-L-lysine adhesion layer (see Methods) and residual cellular Brownian motion in liquid brought the cells closer to the diamond substrate and improved their spatial stability, resulting in higher time-averaged magnetic fields at the layer of NV centres near the diamond surface. We thus expect that the dried cell technique may be the preferred approach for biological applications that do not require sustained imaging of magnetic fields produced by developing cells.

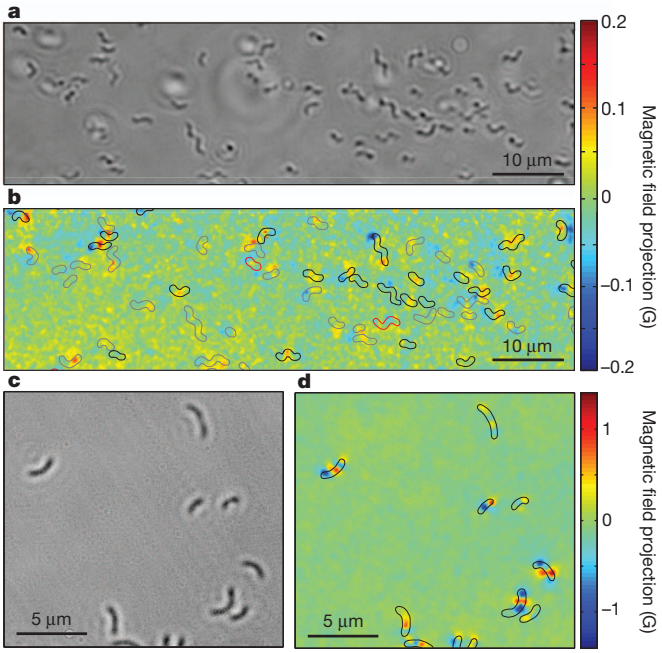

Figure 2 | Wide-field optical and magnetic images of magnetotactic bacteria. a, Bright-field optical image of MTB adhered to the diamond surface while immersed in PBS. **b**, Image of magnetic field projection along the [111] crystallographic axis in the diamond for the same region as **a**, determined from NV ODMR. Superimposed outlines indicate MTB locations determined from **a**. Outline colours indicate results of the live-dead assay performed after measuring the magnetic field (black for living, red for dead, and grey for indeterminate). **c**, Bright-field image of dried MTB on the diamond chip. **d**, Image of magnetic field projection along [111] for the same region, with outlines indicating MTB locations determined from **c**.

As shown in Figs 2–4, the NV-diamond wide-field imager enables rapid, simultaneous measurement of biomagnetic particle distributions in many MTB, with magnetic field sensitivity and spatial resolution sufficient both to localize magnetic nanoparticles within individual MTB and to quantify the MTB magnetic moment from the magnetic field images. To verify these capabilities, we recorded scanning electron microscope (SEM) images of dried MTB in place on the surface of the diamond chip after the magnetic and bright-field imaging had been completed. Positions and relative sizes of the magnetic nanoparticles within each MTB were determined from the backscattered electron SEM images, and used to calculate the expected vector magnetic field pattern from the MTB (up to a normalization constant equivalent to the total magnetic moment of the particles—see Methods). The magnetic field patterns that we calculated (from SEM data) and measured (with the NV-diamond imager) were in excellent agreement (Fig. 3a–h), across a wide variety of magnetic nanoparticle distributions within the MTB (Fig. 4). We also determined the total magnetic moment of each MTB (for example, $(1.2 \pm 0.1) \times 10^{-16}$ A m^2 for the MTB in Fig. 3a–h) by numerically fitting the modelled field distribution to the measured distribution, leaving the standoff distance and magnetic moment as free parameters. From such optical magnetic field measurements, we determined the distribution of magnetic moments from 36 randomly-sampled MTB on the diamond surface (Fig. 3i), with a mean value (0.5×10^{-16} A m^2) that was consistent with previous estimates of the average moment per MTB for *M. magneticum* AMB-1 (ref. 24), although our measurements showed that most AMB-1 cells had smaller moments. Note that most previously applied magnetic measurement techniques determine the average properties of large MTB populations[24,25] but are insensitive to variations among individuals within the population. In contrast, the ability of the NV-diamond

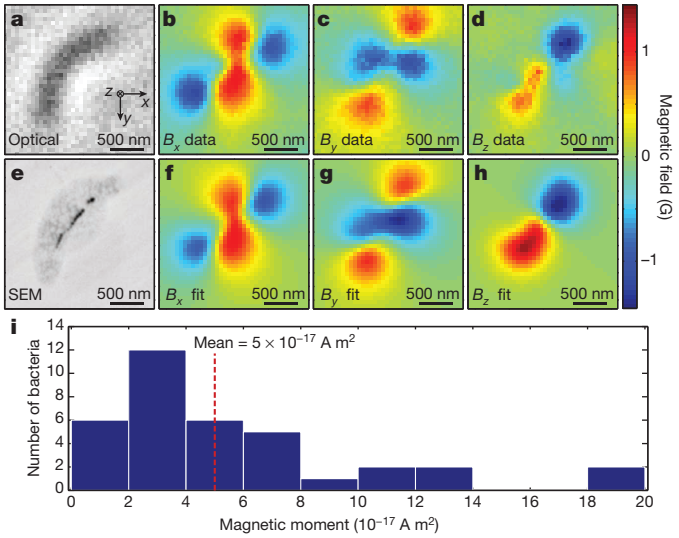

Figure 3 | Determining magnetic moments of individual bacteria from measured magnetic field distributions. **a**, Bright-field image of an MTB. **b–d**, Measured magnetic field projections along the *x* axis (B_x; **b**), *y* axis (B_y; **c**) and *z* axis (B_z; **d**) within the same field-of-view. **e**, Scanning electron microscope (SEM) image of the same bacterium. **f–h**, Simulated magnetic field projections along the *x* axis (**f**), *y* axis (**g**) and *z* axis (**h**), assuming that magnetic nanoparticle locations match those extracted from **e**. The total magnetic moment was determined from the best fit of the calculated field distribution to the measurement (see Methods for details). **i**, Magnetic moments of 36 randomly-sampled MTB, as determined from optical magnetic field images and modelled field distributions.

wide-field magnetic imager to measure rapidly the magnetic properties of many individuals in an MTB population provides a robust tool to investigate the defects of various biomineralization mutants, making it possible to distinguish between defects that equally affect all cells in a population versus those that disproportionately disrupt magnetosome formation in a subset of cells. The *M. magneticum* AMB-1 bacteria studied here provided high signal-to-noise ratio magnetic imaging data, even though the typical magnetic moments of these bacteria are an order of magnitude smaller than many commonly studied MTB strains[3,21]. This suggests that NV magnetic imaging will be applicable to a broad variety of MTB.

Furthermore, we were able to determine the positions of magnetic nanoparticle chains in individual MTB from the magnetic field distributions measured with the NV-diamond imager, even without the use of correlated SEM data, by noting that the magnetic nanoparticle chain endpoints occurred at locations of maximum field divergence (yellow bars in Fig. 4). Distinct groups of magnetic nanoparticles could be resolved if their separation was more than the 400 nm diffraction-limited resolution of our optical magnetometry measurements (for example, Fig. 4d), and endpoints of single, well-isolated magnetic nanoparticle chains could be localized to within <100 nm (for example, Fig. 4b). Using the chain positions and a simplified model for the magnetic nanoparticle field-source distribution, we estimated the total magnetic moments of individual MTB from the magnetic field data alone (without correlated SEM measurements). The magnetic moments determined using this analysis procedure (for example, 0.9×10^{-16} A m^2 for the MTB in Figs 3a–h and 4a, using the estimated chain position in Fig. 4a) agreed well with the values derived using the more detailed SEM-based models when the magnetic nanoparticles were arranged in long chains.

The NV-diamond wide-field imager provides powerful new capabilities that could shed light on unanswered questions regarding the development of MTB magnetic properties[17,18]. Some existing methods can probe the internal magnetic structure of a single MTB[3,19], or measure the magnetic field[20] or field gradient[21] near a single MTB, but only NV magnetic imaging provides direct magnetic field measurements with sub-cellular resolution under ambient environmental conditions—opening the way to real-time imaging of magnetic nanoparticle formation and chain dynamics in single living MTB. Real-time magnetic measurements will enable observation of the transition of magnetic nanoparticles from superparamagnetic to permanent, single-magnetic-domain states as the nanoparticles grow[18]. The ability to locate chains of nanoparticles from the magnetic images will make it possible to measure the movement of magnetosome chains across the cell-division cycle of individual MTB.

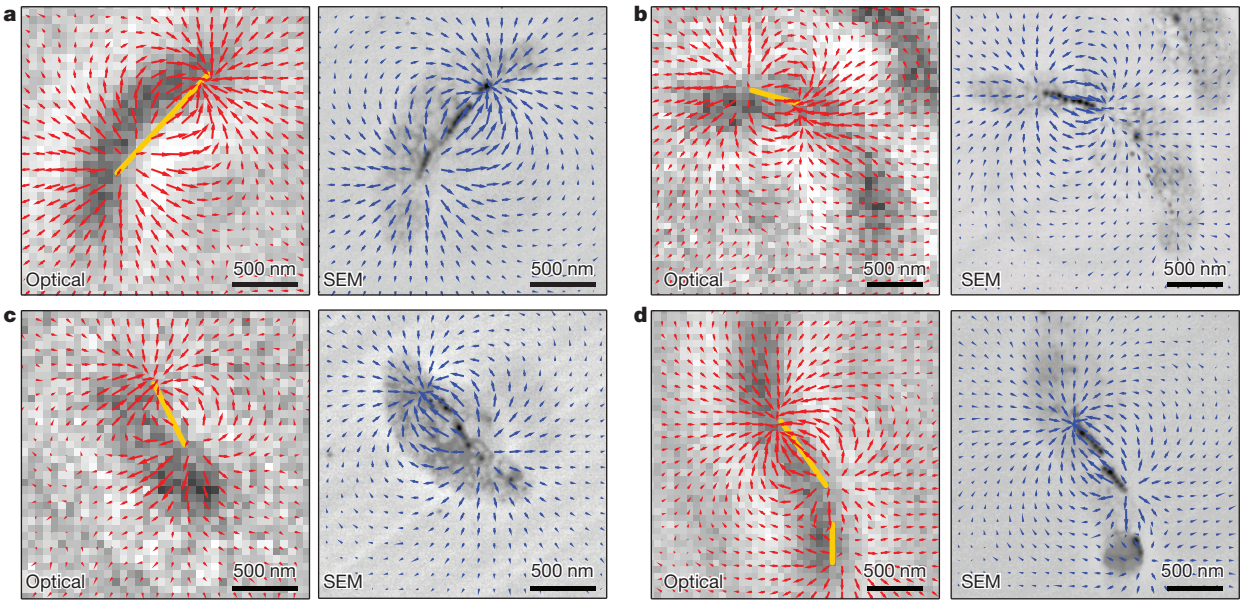

Figure 4 | Localization of magnetic nanoparticle chains using magnetic field measurements. **a**, Vector plots of the measured (red arrows, left panel) and simulated (blue arrows, right panel) magnetic field projections in the *x*–*y* plane, for the same MTB as in Fig. 3a–h, superimposed on the optical and backscattered electron images, respectively. The estimated location of the magnetic nanoparticle chain inside the MTB (yellow bar, left panel), as determined from the divergence of the measured magnetic field, coincides well with the magnetic nanoparticle positions found by SEM. **b–d**, The same information as presented in **a**, but for three different MTB. In **d**, two distinct magnetic nanoparticle chains are identified (yellow bars, left panel).

The measurements presented here are also directly applicable to studying the formation of magnetic nanoparticles in other organisms[26]. Such formation is of interest for MRI contrast enhancement[27], and has been linked with neurodegenerative disorders[28]; it has also been proposed as a mechanism for magnetic navigation in higher organisms[26,29,30]. In particular, there is great current interest in identifying potential vertebrate magnetoreceptor cells[30], which are believed to have a magnetic moment that is comparable to or larger than found in MTB, suggesting that high-throughput NV-diamond magnetic imaging could be a valuable tool for localizing magnetic cells in a broad range of tissue samples. More generally, with further improvements in detector sensitivity and the use of spin-echo techniques for the detection of time-dependent fields[6,7,11], NV-diamond magnetic imaging could be applied to a variety of biologically interesting systems, including firing patterns in neuronal cultures[5,6], detection of free radicals generated by signalling or immune responses, and the localization of molecules tagged with specific spin labels.

METHODS SUMMARY

Wide-field ODMR measurements were acquired of *M. magneticum* AMB-1 bacteria adhered to a diamond chip with a 10-nm-thick layer of NV centres 10 nm from the surface. For wet samples, a thin layer of poly-L-lysine was deposited on the diamond to improve cellular adhesion. A uniform 37-G external magnetic field was applied to separate the $|\pm 1\rangle$ spin states and to select the NV axis of interest. The magnetic-field shifts along the NV axis were extracted by fitting Lorentzian lines to the ODMR signals from each pixel of the image. For wet samples, a fluorescence-based bacterial viability assay (Molecular Probes BacLight kit) was carried out to determine which cells remained alive after imaging. For samples of dried cells, the magnetic imaging was repeated for all four NV axes to create a two-dimensional image of the magnetic field along all three Cartesian directions; the diamond with bacteria was then imaged with a field emission SEM (Zeiss Sigma) using backscatter mode to identify the locations of the magnetosomes within the bacteria. A nonlinear fit was performed on simulated magnetic field images calculated from the positions and sizes of the magnetosomes to find the standoff distance and magnetic moments of the magnetosome chains. Magnetosome chain locations and directions were also estimated using the measured magnetic field divergence, and the magnetic moment of the chain was calculated by modelling each chain as a continuous row of magnetic dipoles.

Full Methods and any associated references are available in the online version of the paper.

Received 4 February; accepted 14 March 2013.

1. Lee, S.-C. *et al.* MR microscopy of micron scale structures. *Magn. Reson. Imaging* **27,** 828–833 (2009).
2. Finkler, A. *et al.* Self-aligned nanoscale SQUID on a tip. *Nano Lett.* **10,** 1046–1049 (2010).
3. Dunin-Borkowski, R. E. *et al.* Magnetic microstructure of magnetotactic bacteria by electron holography. *Science* **282,** 1868–1870 (1998).
4. Degen, C. L., Poggio, M., Mamin, H. J., Rettner, C. T. & Rugar, D. Nanoscale magnetic resonance imaging. *Proc. Natl Acad. Sci. USA* **106,** 1313–1317 (2009).
5. Hall, L. T. *et al.* Monitoring ion-channel function in real time through quantum decoherence. *Proc. Natl Acad. Sci. USA* **107,** 18777–18782 (2010).
6. Pham, L. M. *et al.* Magnetic field imaging with nitrogen-vacancy ensembles. *N. J. Phys.* **13,** 045021 (2011).
7. Maze, J. R. *et al.* Nanoscale magnetic sensing with an individual electronic spin in diamond. *Nature* **455,** 644–647 (2008).
8. Balasubramanian, G. *et al.* Nanoscale imaging magnetometry with diamond spins under ambient conditions. *Nature* **455,** 648–651 (2008).
9. Maletinsky, P. *et al.* A robust scanning diamond sensor for nanoscale imaging with single nitrogen-vacancy centres. *Nature Nanotechnol.* **7,** 320–324 (2012).
10. Steinert, S. *et al.* High sensitivity magnetic imaging using an array of spins in diamond. *Rev. Sci. Instrum.* **81,** 043705 (2010).
11. Le Sage, D. *et al.* Efficient photon detection from color centers in a diamond optical waveguide. *Phys. Rev. B* **85,** 121202(R) (2012).
12. Hanson, R., Mendoza, F. M., Epstein, R. J. & Awschalom, D. D. Polarization and readout of coupled single spins in diamond. *Phys. Rev. Lett.* **97,** 087601 (2006).
13. Childress, L. *et al.* Coherent dynamics of coupled electron and nuclear spin qubits in diamond. *Science* **314,** 281–285 (2006).
14. Mamin, H. J. *et al.* Nanoscale nuclear magnetic resonance with a nitrogen-vacancy spin sensor. *Science* **339,** 557–560 (2013).
15. Staudacher, T. *et al.* Nuclear magnetic resonance spectroscopy on a (5-nanometer)^3 sample volume. *Science* **339,** 561–563 (2013).
16. Grinolds, M. S. *et al.* Nanoscale magnetic imaging of a single electron spin under ambient conditions. *Nature Phys.* **9,** 215–219 (2013).
17. Komeili, A. Molecular mechanisms of compartmentalization and biomineralization in magnetotactic bacteria. *FEMS Microbiol. Rev.* **36,** 232–255 (2012).
18. Faivre, D. & Schüler, D. Magnetotactic bacteria and magnetosomes. *Chem. Rev.* **108,** 4875–4898 (2008).
19. Lam, K. P. *et al.* Characterizing magnetism of individual magnetosomes by X-ray magnetic circular dichroism in a scanning transmission X-ray microscope. *Chem. Geol.* **270,** 110–116 (2010).
20. Qian, L. *et al.* Magnetic characterization of individual magnetotactic bacteria. (APS March Meeting 2011, 2011); http://meetings.aps.org/link/BAPS.2011.MAR.D16.8 (abstract published online, 2011).
21. Proksch, R. B. *et al.* Magnetic force microscopy of the submicron magnetic assembly in a magnetotactic bacterium. *Appl. Phys. Lett.* **66,** 2582–2584 (1995).
22. Matsunaga, T., Suzuki, T., Tanaka, M. & Arakaki, A. Molecular analysis of magnetotactic bacteria and development of functional bacterial magnetic particles for nano-biotechnology. *Trends Biotechnol.* **25,** 182–188 (2007).
23. Draper, O. *et al.* MamK, a bacterial actin, forms dynamic filaments *in vivo* that are regulated by the acidic proteins MamJ and LimJ. *Mol. Microbiol.* **82,** 342–354 (2011).
24. Krichevsky, A. *et al.* Trapping motile magnetotactic bacteria with a magnetic recording head. *J. Appl. Phys.* **101,** 014701 (2007).
25. Moskowitz, B. M., Frankel, R. B. & Bazylinski, D. A. Rock magnetic criteria for the detection of biogenic magnetite. *Earth Planet. Sci. Lett.* **120,** 283–300 (1993).
26. Pósfai, M. & Dunin-Borkowski, R. E. Magnetic nanocrystals in organisms. *Elements* **5,** 235–240 (2009).
27. Zurkiya, O., Chan, A. W. S. & Hu, X. Mag A is sufficient for producing magnetic nanoparticles in mammalian cells, making it an MRI reporter. *Magn. Reson. Med.* **59,** 1225–1231 (2008).
28. Dobson, J. Magnetic iron compounds in neurological disorders. *Ann. NY Acad. Sci.* **1012,** 183–192 (2004).
29. Mora, C. V., Davison, M., Wild, J. M. & Walker, M. M. Magnetoreception and its trigeminal mediation in the homing pigeon. *Nature* **432,** 508–511 (2004).
30. Eder, S. H. K. *et al.* Magnetic characterization of isolated candidate vertebrate magnetoreceptor cells. *Proc. Natl Acad. Sci. USA* **109,** 12022–12027 (2012).

Supplementary Information is available in the online version of the paper.

Acknowledgements We thank L. Qian for discussions about related experiments using a scanning SQUID microscope in the laboratory of K. A. Moler, J. W. Lichtman and R. Schalek for access to the SEM, S. G. Turney for access to the water-immersion objective and advice regarding cell immobilization, and P. R. Hemmer and H. Park for technical discussions. A.K. was supported by a David and Lucille Packard Foundation Fellowship in Science and Engineering and by the National Institutes of Health (R01GM084122). This work was supported by the NSF and the DARPA QuASAR programme.

Author Contributions D.L. and R.L.W. conceived the idea of the study. K.A. developed modelling and fitting algorithms to interpret the data. D.L., K.A., D.R.G., S.J.D. and L.M.P. performed magnetic, optical and SEM imaging experiments, and analysed data. L.R.-L. and A.K. provided bacteria cultures and TEM images. M.D.L., R.L.W. and A.Y conceived the application of the NV-diamond wide-field imager to biomagnetism. All authors discussed the results and participated in writing the manuscript.

Author Information Reprints and permissions information is available at www.nature.com/reprints. The authors declare no competing financial interests. Readers are welcome to comment on the online version of the paper. Correspondence and requests for materials should be addressed to R.L.W. (rwalsworth@cfa.harvard.edu).

METHODS

NV physics. The NV centre consists of a substitutional nitrogen atom adjacent to a vacancy in the diamond lattice (see Supplementary Fig. 1). The NV centre has a spin-triplet ground state with a 2.87 GHz zero-field splitting between the $|0\rangle$ and $|\pm1\rangle$ spin states (see Fig. 1b). Optical excitation of an NV centre primarily produces a spin-conserving excitation and decay process, resulting in the emission of a photon in the 640–800 nm wavelength band. However, the $|\pm1\rangle$ excited states also decay non-radiatively about one-third of the time to the $|0\rangle$ ground state via metastable singlet states. This leads to both optical polarization into the $|0\rangle$ ground state and state-dependent fluorescence rates that may be used to optically distinguish the $|0\rangle$ state from the $|\pm1\rangle$ states.

The magnetic field projection at an NV centre's location can be measured by monitoring the fluorescence rate of the NV centre during continuous optical excitation, while varying the frequency of a continuous microwave drive[8–10]. When the applied microwave frequency is on resonance with either of the $|0\rangle \leftrightarrow |\pm1\rangle$ state transitions, some of the NV state population is transferred from the $|0\rangle$ optically-pumped state to a mixed state, and consequently, the fluorescence rate decreases.

The NV centre's zero-field splitting quantizes the spin states along the NV symmetry axis (indicated by a blue rod in Supplementary Fig. 1). Depending upon the relative positions of the nitrogen atom and vacancy, this symmetry axis can lie along one of four possible crystallographic directions within the diamond lattice (other possible crystallographic axes are indicated by yellow rods in Supplementary Fig. 1). In an external magnetic field, the $|0\rangle \leftrightarrow |\pm1\rangle$ spin-flip transition frequencies shift by $\Delta f = \pm\gamma B_{||}$ (see Fig. 1c), where $\gamma = 2.8\,\mathrm{MHz\,G^{-1}}$ is the gyromagnetic ratio of the NV electronic spin, and $B_{||}$ is the magnetic field projection along the NV symmetry axis.

Diamond samples. Magnetic field sensing was carried out using high-purity, single-crystal diamond chips. For imaging wet bacterial samples, we used an electronic-grade diamond (3 mm × 3 mm × 0.5 mm) grown using chemical vapour deposition (CVD) by Element Six Ltd. The diamond was implanted with $^{15}N^{+}$ ions at 14 keV energy and annealed at 1,200 °C to produce a 10-nm-thick layer of NV centres 20 nm beneath the surface of the diamond (as estimated using Stopping and Range of Ions in Matter (SRIM) software). The estimated NV surface density within the layer was 3×10^{11} NV per cm^2. For imaging dry bacterial samples, we used a high-purity, single-crystal diamond chip (1.5 mm × 1.5 mm × 0.3 mm) manufactured by Sumitomo Electric Industries using the high-pressure, high-temperature (HPHT) method. This diamond was implanted with $^{15}N^{+}_{2}$ ions with 15 keV energy and then annealed at 800 °C to produce a 10-nm-thick layer of NV centres 10 nm beneath the surface of the diamond (as estimated using SRIM), with an estimated surface density of 1×10^{12} NV per cm^2.

Wide-field magnetic imaging microscope. NV centres were optically excited with a 532 nm laser (Changchun New Industries) switched on and off by an acousto-optic modulator (Isomet, M1133-aQ80L-1.5). A small fraction of the laser light was split off and directed onto a photodiode (Thorlabs), and the resulting signal was sent to a servo-lock system (New Focus) to amplitude-stabilize the excitation beam using the same acousto-optic modulator. For imaging of bacterial samples in liquid, laser light was coupled into the diamond from below through a polished glass cube (constructed from two right-angle prisms, Thorlabs), to which the diamond was affixed by optical adhesive (Norland). The peak intensity of the totally-internally-reflected laser light at the interior surface of the diamond was measured in this case to be $\sim 1\,\mathrm{kW\,cm^{-2}}$. We also note that for our angle of incidence at the diamond–water interface, $\theta_{dw} \approx 39^{\circ}$, the calculated attenuation length for the evanescent wave intensity is $d_{dw} = 58$ nm. For imaging of dry samples, laser light could be configured in the same manner as for live/wet samples, or directed onto the bacteria from below, normal to the diamond surface. Dry sample data presented here were acquired using the latter method.

A 660-nm-wavelength LED (Thorlabs) was used to back-illuminate the sample for bright-field images. Excitation of fluorescence dyes used in the bacterial viability assays (see below) was carried out with a 470-nm LED (Thorlabs), directed onto the sample through the microscope objective. Optical fluorescence or transmitted red LED light was collected by the objective (Olympus, UIS2 LumFLN 60xW /1.1 NA for wet samples; Olympus, MPlan FLN 100×/0.90 NA for dry samples), passed through a dichroic mirror (Thorlabs for wet samples; Semrock for dry samples) and an optical filter (Semrock for NV fluorescence and transmitted red light; emission filters as described below for fluorescence from bacterial viability assay dyes), and imaged onto a digital camera (Andor for wet samples; Starlight Xpress for dry samples). The output of a microwave synthesizer (SRS) was controlled by a switch (Mini-Circuits), then amplified (Mini-Circuits) and applied to the diamond with a wire. A permanent magnet was used to apply a uniform external magnetic field.

ODMR measurements. *M. magneticum* AMB-1 cells were grown statically in 1.5-ml microcentrifuge tubes filled with 1.5 ml of growth medium (described in ref. 31, but with 0.1 g l^{-1} of sodium thiosulphate). For measurements of wet samples, the diamond surface was prepared by placing a drop (~5 µl) of 0.01% poly-L-lysine solution (Sigma molecular mass 70–150 kDa) on its surface, which was then allowed to dry. The bath around the diamond (contained in a chamber consisting of a cut microcentrifuge tube glued to the glass mounting surface, volume ~200 µl) was filled with 50 µl of bacterial solution, and topped up with PBS. For dry measurements, a drop of bacterial solution was placed directly on the diamond above the NV layer, allowed to dry, rinsed with deionized water, and dried a second time. The sample was then placed in the imager with the active diamond surface facing the objective. A uniform 37-G external magnetic field was applied along a single NV axis to distinguish it from the other three NV axes. This magnetic field strength was an order of magnitude less than the coercive field typically required to flip the magnetic orientation of MTB[3,21], and we found that the magnetization of the MTB described here remained fixed as the external field was varied.

ODMR[8–10] spectra were measured by imaging NV fluorescence from the whole field-of-view at different microwave frequency values. The typical total fluorescence collection time was 4 min for both wet and dry bacterial samples. For each pixel, Lorentzian fits were applied to the ODMR spectra and the magnetic field shifts along the NV axis were extracted. This procedure was repeated with the external field applied along each of the four NV axes, which in turn allowed the vector magnetic field in the NV layer to be determined for all three Cartesian directions across the field-of-view. For magnetic fields B_1 to B_4, corresponding to measurements along axes 1 to 4, respectively, the fields in the Cartesian coordinates were calculated from

$$B_x = (3/2)^{1/2}(B_2 - B_4)/2,$$

$$B_y = (3/2)^{1/2}(B_1 - B_3)/2,$$

$$B_z = 3^{1/2}(-B_1 - B_2 - B_3 - B_4)/4$$

Bacterial viability assay. Immediately after magnetic field imaging of wet samples, the viability of the bacteria was determined in place on the diamond surface using a standard fluorescence-based live-dead assay (Molecular Probes, BacLight kit). A mixture of the fluorescent nucleic acid stains SYTO 9 (final concentration 5 µM) and propidium iodide (final concentration 30 µM) was added to the bath, and bright-field images were immediately collected to verify that the positions of the bacteria on the diamond surface were not perturbed. The sample was then incubated in the dark for 15 min, and fluorescence images were collected by exciting with a LED at 470 nm (Thorlabs). Green SYTO-9 fluorescence and red propidium iodide fluorescence were collected successively using appropriate emission filters (Thorlabs for green; Chroma for red). Custom software was used to co-register the resulting fluorescence images and perform rolling-ball background subtraction, and a peak-finding algorithm was applied to determine the positions of the bacteria. The ratio of red to green fluorescence intensity, integrated over each cell, was calculated and compared to a live/dead calibration performed previously under the same conditions (see Supplementary Information for details). MTB with a fluorescence ratio less than 0.5 were taken to be alive, while those with a fluorescence ratio greater than 1.0 were assigned as dead. Bacteria with intermediate fluorescence ratios between 0.5 and 1.0 could not be assigned to either category with high certainty based on assay calibration measurements, and were therefore labelled as indeterminate in experimental data.

Before collecting the data displayed in Fig. 2, we carried out a series of preliminary live-dead assays, including the calibrations described in Supplementary Methods. These assays revealed that, even after a full hour of exposure to $f \approx 2.88$ GHz microwave fields at the intensities used in our ODMR measurements, the fraction of bacteria remaining alive was essentially the same as that in unperturbed samples immediately after they were taken from culture. This suggests that any bacterial fatality during experiments was the result of residual evanescent coupling of laser light through the diamond surface. These observations were consistent with direct measurements of the bath temperature when microwave power was applied, which showed only a modest increase of 1–2 °C above room temperature.

Electron microscopy. After magnetic field measurements were completed on dried samples, imaging was performed with a field emission SEM (Zeiss Sigma). The diamond substrate and intact bacteria were carbon-coated in a thermal evaporator (Edwards Auto 306) and mounted on silicon wafers using copper tape. The bacteria were imaged without dehydration or fixation. Images of magnetic nanoparticles were obtained using backscatter mode, at ×30,000 magnification and with an accelerating voltage of 8 kV. The TEM image in Fig. 1d was recorded using the procedure outlined in ref. 32.

Fitting the magnetic field of an MTB. Magnetic field patterns of the bacteria were fitted with a constrained model using SEM measurements of the relative sizes and positions of the magnetic nanoparticles, with standoff distance from the diamond and magnetic moment scaling factors left as free parameters. First, a peak-finding algorithm was applied to locate magnetic nanoparticles in the image. Magnetic nanoparticle chains were determined by assigning two adjacent magnetic nanoparticles to the same chain if their separation was less than 120 nm. For each chain, the orientation of the magnetic moment in the plane of the diamond surface was determined using a linear fit to the magnetic nanoparticle positions. Gaussian curves were fitted to the SEM images of each magnetic nanoparticle along the direction perpendicular to the axis of the chain, and the fit amplitudes were used to assign relative magnetic moment densities along the chain. Each magnetic nanoparticle in a chain was assumed to act as a point dipole with the same magnetic moment direction as its chain. (This approximation was motivated by the observation of highly aligned magnetic nanoparticle dipoles in previous work (see, for example, refs 3, 19.) In some cases, individual magnetic nanoparticle were further than 120 nm from any chains; their dipole moment was estimated to be in the same direction as that of the nearest chain.

Next, a nonlinear fit routine using the Levenberg–Marquardt algorithm was performed to match simulated magnetic field images with those measured. The simulation first calculated the three components of the magnetic field on the diamond surface using the positions, directions and relative magnetic strengths of each magnetic nanoparticle. The ODMR signal for all NV axes was then calculated for each pixel, and these signals were convolved with a point-spread function (full-width at half-maximum of 400 nm) to create simulated ODMR fluorescence data. As in the case of the measured data, images of B_x, B_y and B_z were reconstructed on a pixel-by-pixel basis from the frequency shifts for the four NV axes extracted from Lorentzian fits. The algorithm was run independently to minimize x and y position offsets of the SEM images as well as the standoff distance from the diamond surface. Generally, B_x images were used for the fitting. Finally, the overall magnetic moment was calculated on a pixel-by-pixel basis for the best-fit geometry, and the optimal value was determined by least-squares fitting to the measured data. The best-fit magnetic moment did not depend strongly on the value of the best-fit standoff distance for typical distances of 100–200 nm, owing to convolution of the NV fluorescence signal with the ~400-nm point spread function of the optical microscope. We note that this method cannot recover exact dipole orientations, particularly for isolated magnetic nanoparticles. Nevertheless, the overall magnetic moment is dominated by contributions from long chains, whose field patterns are well-described by this method.

Estimating magnetic properties directly from ODMR. In cases where magnetic nanoparticles were organized into ordered chains that were well-approximated by finite solenoids, the chain positions and magnetic moments could be determined even without comparison to SEM data. Chain locations and orientations were estimated from the measured magnetic field divergence in the diamond plane ($\partial B_x/\partial x + \partial B_y/\partial y$) by assigning chain endpoints to the local maxima and minima of the divergence. (The maximum precision of this estimate is given approximately by the diffraction-limited resolution of the ODMR measurement divided by the signal-to-noise ratio of the calculated magnetic field divergence, which is approximately 40 nm.) The chain was then approximated as a continuous line of magnetic dipoles, which can be shown to have the same field as a magnetic source and sink separated by the chain length (that is, a narrow finite solenoid). This provided a simple way to calculate B_z just below the chain. The magnetic moment could then be determined directly by spatially integrating the absolute value of B_z across the diamond surface. This integrated value is independent of standoff distance when the chain length is much larger than the standoff distance and the diameter of the field-of-view is much larger than the chain length. Moreover, it is independent of the point-spread function of the microscope objective.

31. Komeili, A., Vali, H., Beveridge, T. J. & Newman, D. K. Magnetosome vesicles are present before magnetite formation, and MamA is required for their activation. *Proc. Natl Acad. Sci. USA* **101,** 3839–3844 (2004).
32. Murat, D., Quinlan, A., Vali, H. & Komeili, A. Comprehensive genetic dissection of the magnetosome gene island reveals the step-wise assembly of a prokaryotic organelle. *Proc. Natl Acad. Sci. USA* **107,** 5593–5598 (2010).